Tellus SERIES B CHEMICAL AND PHYSICAL METEOROLOGY
PUBLISHED BY THE INTERNATIONAL METEOROLOGICAL INSTITUTE IN STOCKHOLM

Tellus (2009), 61B, 64–78
Printed in Singapore. All rights reserved

TELLUS

In situ measurements of optical properties at Tinfou (Morocco) during the Saharan Mineral Dust Experiment SAMUM 2006

By A. SCHLADITZ[1]*, T. MÜLLER[1], N. KAADEN[1], A. MASSLING[1,2], K. KANDLER[3], M. EBERT[3], S. WEINBRUCH[3], C. DEUTSCHER[4] and A. WIEDENSOHLER[1], [1]*Leibniz Institute for Tropospheric Research, Leipzig, Germany;* [2]*National Environmental Research Institute, Aarhus University, Roskilde, Denmark;* [3]*Institute for Applied Geosciences – Environmental Mineralogy, Technical University Darmstadt, Germany;* [4]*Institute for Atmospheric Physics, Johannes -Gutenberg -University, Mainz, Germany*

(Manuscript received 25 January 2008, in final form 12 September 2008)

ABSTRACT

In situ measurements of optical and physical properties of mineral dust were performed at the outskirts of the Saharan Desert in the framework of the Saharan Mineral Dust Experiment part 1 (SAMUM-1). Goals of the field study were to achieve information on the extent and composition of the dust particle size distribution and the optical properties of dust at the ground. For the particle number size distribution, measured with a DMPS/APS, a size dependent dynamic shape factor was considered. The mean refractive index of the particles in this field study is $1.53–4.1 \times 10^{-3}i$ at 537 nm wavelength and $1.53–3.1 \times 10^{-3}i$ at 637 nm wavelength derived from measurements of scattering and absorption coefficients, as well as the particle size distribution. Whereas the real part of the refractive index is rather constant, the imaginary part varies depending on the mineral dust concentrations. For high dust concentration the single scattering albedo is primarily influenced by iron oxide and is 0.96 ± 0.02 and 0.98 ± 0.01 at 537 nm and 637 nm wavelength, respectively. During low dust concentration the single scattering albedo is more influenced by a soot-type absorber and is 0.89 ± 0.02 and 0.93 ± 0.01 for the same wavelengths.

1. Introduction

Climate forcing of the atmosphere is an important research subject in natural science. Whereas climate forcing of greenhouse gases in the atmosphere is rather well known, the influence of the aerosol is much less understood.

The Sahara Desert is globally one of the largest natural sources of mineral dust particles. Its source strength varies between 130 and 760 Tg yr^{-1} (Goudie and Middleton, 2001). Satellite observations from Moderate Resolution Imaging Spectroradiometer (MODIS) and recently also from Cloud- Aerosol Lidar and Infrared Pathfinder Satellite Observation (Calipso) show dust plumes spreading from North Africa over the Atlantic Ocean (Kaufman et al., 2002; Luo et al., 2003; Kaufman et al., 2005; Engelstaedter et al., 2006). On its transport over hundreds to thousands of kilometres, the Saharan mineral dust influences the radiation balance of the atmosphere. The phenomenon of high dust emissions from northwest Africa shows an increase in dust activity from March onwards and subsiding in September (Engelstaedter et al., 2006).

In mineral dust, the main absorbers are iron oxides, such as hematite and goethite (Lafon et al., 2004). Both compounds absorb sunlight in the UV and with lower efficiency in the visible spectral range (Horvath, 1993). Hematite and Goethite have similar optical properties (Balkanski et al., 2007). Hematite has a characteristic increase of the imaginary part of the refractive index (Hsu and Matijevic, 1985; Bedidi and Cervelle, 1993; Sokolik and Toon, 1999) near 550 nm with decreasing wavelengths. Linke et al. (2006) derived that a Morocco soil-sample contained a hematite mass fraction of 0.6% for the dust particles $<20\,\mu$m.

Radiation model simulations show that the impact of mineral dust to the atmospheric radiation budget is highly variable depending on the albedo of the underlying surface, cloudiness, optical properties and vertical distribution of the dust particles (Tegen et al., 1996; Liao and Seinfeld, 1998). However, even the sign of the radiative forcing of the mineral aerosols in a global meaning is uncertain (Tegen et al., 1996; Sokolik and

*Corresponding author.
e-mail: schladitz@tropos.de
DOI: 10.1111/j.1600-0889.2008.00397.x

Toon, 1999). Altogether, there are still open scientific questions concerning mineral dust. To answer some of these questions, the SAharan Mineral dUst experiMent 1 (SAMUM-1) field experiment was performed in Morocco from May to June 2006. It was attempted to characterize the Saharan dust at Ouarzazate (30°54′N; 6°54′W; 1133 m height above sea level, a.s.l.) and near the small village Tinfou (30°15′N; 5°37′W; 730 m height a.s.l.) at the outskirts of the Sahara Desert. In the following, the described measurements were conducted at the Tinfou ground station. A measurement container of the Leibniz Institute for Tropospheric Research (IfT) served as an air-conditioned laboratory with distinct instrumentation for measurement of hygroscopic and optical properties, and particle number size distribution.

The particle number size distribution in the size range between 20 nm to 10 μm was measured and characterized at the ground. These measurements completed the ambient size distribution measurements presented in Kandler et al. (2008). Particle number size distribution measurements were performed at the ground for Saharan dust for a long time period together with a high temporal resolution. This paper provides optical parameters such as the single scattering albedo and the complex refractive index for the Saharan aerosol in the source region. Within a closure study, we varied the complex refractive index until measured and calculated optical parameters agreed within their uncertainties. In addition to overall average values, the particle number size distribution and key optical parameters were considered for low, medium and high Saharan mineral dust concentrations at the ground. Correlations are discussed between the effective radius and the single scattering albedo as well as the imaginary part of the refractive index. To answer the important question of the main absorbing and non-absorbing components of Saharan aerosol, results of the single particle analysis presented in Kandler et al. (2008) are considered. Furthermore, the influence of the wind speed on optical properties is discussed in this investigation.

Other SAMUM-1 contributions about in-situ optical properties have focus, for example, on the spectral behaviour of the pure dust refractive index and absorption coefficients (Müller et al., 2008) and optical properties of different dust layers from aircraft-based measurements (Petzold et al., 2008).

2. Measurements and data evaluation

2.1. In situ measurements

A PM_{10} inlet was mounted 2 m above the roof of the container laboratory upstream of the measurement devices. Inside the container the aerosol flow was iso-kinetically split to provide a representative aerosol to the aerosol instrumentation. The relative humidity of the sample aerosol was relatively low (RH $\sim$ 20%) and additionally dried either with Nafion® dryer or diffusion dryers to avoid water uptake of aerosol particles in the air-conditioned container. The measurements were conducted at a stable temperature of 295 K. The ambient atmospheric pressure was relatively constant around 930 hPa.

An Aerodynamic Particle Sizer (APS) and a Differential Mobility Particle Sizer (DMPS) have been used to measure the particle number size distributions behind the PM_{10} inlet, without bendings and horizontal aerosol tubes to avoid losses in the sampling line. Due to a limit of space inside the container, the optic rack housing an integrating nephelometer, a Particle Soot Absorption Photometer (PSAP), and a Multi Angle Absorption Photometer (MAAP) was placed with a horizontal distance of 2 m to the PM_{10} inlet. Due to losses of supermicrometre particles, the cut-off diameter PM_x was smaller than directly behind the PM_{10} inlet. An Hygroscopicity-Differential Mobility Analyser-Aerodynamic Particle Sizer (H-DMA-APS) (Leinert and Wiedensohler, 2008) was placed next to the optic rack. The H-DMA-APS combines a Differential Mobility Analyser (DMA) and an APS in one system. During dry conditions (no particle humidification) mobility diameters of 800, 1000 and 1200 nm were selected and classified by their aerodynamic particle diameter with an APS. Losses within the H-DMA-APS were not considered, because the system determines the relative amount of hygroscopic particles in the supermicrometre size range.

An integrating nephelometer (model 3563, TSI Inc., St. Paul, USA) with three wavelengths (λ = 450, 550 and 700 nm) was used to measure a value that is strongly related to the light scattering and hemispheric backscattering coefficients. Due to the design, only scattered light from particles and molecules in the angular range of approximately 7°–170° (Anderson et al., 1996) is detected by the photomultiplier. The ensuing truncation error increases with particle size and is discussed in Heintzenberg et al. (2006) and Heintzenberg and Quenzel (1973). The integrating nephelometer is described in detail in e.g., Anderson et al. (1996) and Anderson and Ogren (1998). To ensure reliable measurement conditions, the integrating nephelometer was calibrated using carbon dioxide and filtered air once before and twice after the field study. Zero measurements using particle free air were conducted each day.

The particulate absorption coefficient was determined using a PSAP (Radiance Research, Seattle, USA) at λ = 537 nm and a MAAP (Thermo Fisher Scientific Inc., Waltham, USA) at λ = 637 nm.

Particle number size distributions were obtained using a combination of a closed loop (Jokinen and Mäkelä, 1997) Differential Mobility Particle Sizer (DMPS) (Birmili et al., 1999) for the mobility size range from 20 to 800 nm and an Aerodynamic Particle Sizer (APS) (model 3321, TSI Inc., St Paul, USA) for the aerodynamic size range from 850 nm to 10 μm. Aerosol and sheath-air flows were checked frequently during the campaign. The APS was calibrated after the field study by the manufacturer TSI Inc., with spherical latex particles of known density and size

to identify shifts in diameter sizing. They have been found no shifts in diameter.

2.2. Uncertainties of the individual instruments

Uncertainties of intensive quantities such as backscatter ratio and single scattering albedo are calculated by propagation of errors using the measurement uncertainty of the extensive quantities such as scattering coefficient, hemispheric backscattering coefficient, and absorption coefficient, as well as the particle number size distribution.

Wex et al. (2002) give an overview about uncertainties of several extensive quantities mentioned above. Anderson et al. (1996) and Anderson and Ogren (1998) give an uncertainty of 7% for the nephelometer-measured scattering and hemispheric backscattering coefficient. The uncertainty for the PSAP reported by Bond et al. (1999) is 6% after flow and filter spot correction. Applying the propagation of errors rule, the absorption coefficient has an error of about 35% after correction of the cross sensitivity to particle scattering. This high value is caused by the rather high uncertainty of the scattering correction, which is $2 \pm 2\%$. This high uncertainty was given by Bond et al. (1999). The error of the absorption coefficient at 537 nm after correction for filter loading (Section 2.3.2) was not quantified. The measurement uncertainty of 12% for the absorption coefficient at 637 nm measured with the MAAP is given by Petzold and Schönlinner (2004). Petzold et al. (2005) point out that the MAAP measures an apparent absorption coefficient that is up to 3% of the extinction coefficient, using non-absorbing aerosol particles.

To estimate the error of the particle number size distribution, the counting errors of the APS and the DMPS have to be taken into account. The error due to counting statistics at low concentrations (no particle coincidence) is 10% (e.g. Heintzenberg et al., 1998) for the APS. The error for the DMPS size range is 12%. The latter value comprises estimates of the counting error of the Condensation Particle Counter (CPC) (model 3760A, TSI Inc., St. Paul, USA) and the flow (aerosol and sheath air) regulation in the DMA.

Varying the extensive quantities in the range of their uncertainty and executing the calculations as described in Section 3.1, the uncertainty of the imaginary parts of the refractive index was derived and stated in Table 2 in parentheses.

2.3. Evaluation of the measurements

2.3.1. Particle number size distribution. It is common to convert the result of the number size distribution measurements to the volume equivalent particle diameter (dp_{ve}). For that purpose, the knowledge of the particle density ρ_p and the dry dynamic shape factor χ_{dry} is necessary. Formulas (1a) and (1b) (e.g. Hinds, 1999; Decarlo et al., 2004) describe the conversion from the aerodynamic particle diameter dp_a and the mobility diameter d_m, respectively, to the volume equivalent particle diameter.

Table 1. Grand average $\overline{\chi_{\mathrm{dry}}}$ and standard deviation (~95% confidence level) of dynamic shape factors for aerodynamic, mobility and volume equivalent particle diameter with a particle density of 2.7 g cm^{-3}

dp_a (nm)	dp_m (nm)	dp_{ve} (nm)	$\overline{\chi_{\mathrm{dry}}}$	$\sigma(\overline{\chi_{\mathrm{dry}}})$
1035	800	681	1.17	0.06
1209	1000	816	1.23	0.08
1399	1200	956	1.26	0.06

$$dp_m = dp_{ve} \cdot \chi_{\mathrm{dry}}, \tag{1a}$$

$$dp_a = dp_{ve}\sqrt{\frac{\rho_p}{\rho_0 \cdot \chi_{\mathrm{dry}}}}. \tag{1b}$$

The overwhelming majority of the supermicrometre particles consists of quartz and silicates (Kandler et al., 2008). Electron microscopy analysis of single particles stated an average particle density of 2.7 g cm^{-3} for particles larger than 500 nm (Kandler et al., 2008). This particle density is similar with the particle density found for a soil-sample from Morocco (Linke et al., 2006) and was also utilized for calculations for the Saharan Dust Experiment (SHADE) (Haywood et al., 2001).

The dry dynamic shape factors χ_{dry} were derived from the H-DMA-APS. Dry dynamic shape factors were derived using eqs. (1a) and (1b) and the particle density given above. A detailed description of this method is given in (Kaaden et al., 2008). The measured shape factors are nearly normally distributed. Shape factors and their standard deviation are shown in Table 1 for three different particle diameters. Note that the relative standard deviation of shape factors of 4.5–6.5% for the entire field campaign was very small. This result emphasizes the good reproducibility of shape factors and their very small variation during the campaign.

By interpolation and extrapolation a distinct shape factor for each particle size in the size range from 550 nm to 1 μm can be given, whereas the shape factor is one for particle diameters up to 550 nm (Kaaden et al., 2008). For the supermicrometre size range a constant shape factor of 1.26 was assumed.

The multiple charge inversion routine, which transforms the mobility distribution into the true particle number size distribution was described by Stratmann and Wiedensohler (1996). This inversion algorithm accounts for multicharged particles in that size range, where the mobility distributions were measured by the DMPS. Particles larger than the size range covered by the DMPS, influence however the derived particle number size distribution, if they are not physically removed upstream of the instrument. These particles carrying a multiple number of charges after passing the bipolar diffusion charger upstream of the DMA were classified erroneously in the particle mobility distribution. They misleadingly remain in the particle number mobility

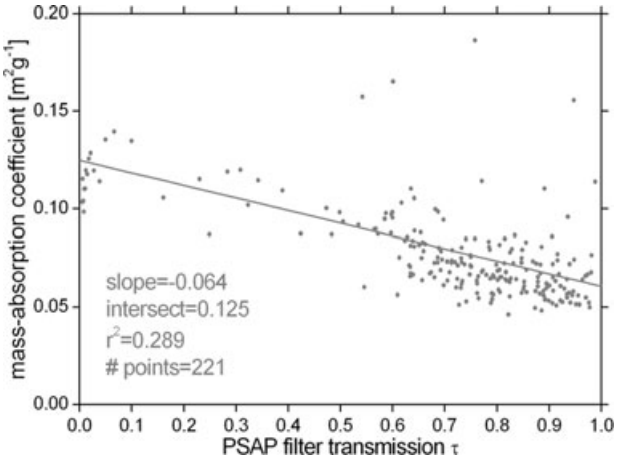

Fig. 1. Mass-absorption coefficient (absorption coefficient $> 5\,\mathrm{Mm}^{-1}$) at 537 nm versus filter transmission of the PSAP. Parameters of linear fits and the respective coefficient of determination (r^2) are added.

distribution after execution of the inversion routine. Sensitivity studies of our own investigation have shown a correction for the particle number mobility distribution is necessary for particle number concentrations more than $50\,\mathrm{cm}^{-3}$ for 1-μm particles. From the simultaneously measured particle number size distributions by the APS, the multiply charged particles were calculated and then removed from the particle mobility distribution.

2.3.2. Absorption coefficient. The apparent absorption coefficient derived by the PSAP was corrected for the scattering artefact, the deposition spot size and the volume aerosol-flowrate as described in Bond et al. (1999). The volume aerosol-flowrate through the PSAP was checked periodically using a bubble flowmeter. After applying these corrections, a loading effect was detected. With decreasing filter transmission, the mass-absorption coefficient

$$\alpha_a = \frac{\sigma_{a,PM_x}}{M}, \tag{2}$$

where σ_{a,PM_x} is the measured absorption coefficient and M the particle mass concentration at PM_x, increases (Fig. 1). In Fig. 1, all absorption coefficients larger than $5\,\mathrm{Mm}^{-1}$ were used. Nevertheless, the correction presented by Bond et al. (1999) is valid for filter transmissions larger than 0.7. For further considerations, values of the absorption coefficient from PSAP measurements were thus disregarded, if the filter transmission was below 0.7. A further method, which corrects the loading effect is described in detail by (Müller et al., 2008). Note, to derive the particle number size distribution and hereupon the particle mass at the optic rack (PM_x) line losses through horizontal pipes and bendings were accounted for. Due to laminar transport (Reynolds number below 2000) of the aerosol inside the pipes, a set of theoretical formulas (Brockmann, 1993) for laminar air flows was used.

3. Calculations

To calculate the nephelometer scattering and absorption efficiencies at PM_x a FORTRAN Mie-code (Bohren and Huffman, 1983) was used. The calculations were done assuming homogeneous, spherical particles at $\lambda = 537$ and 637 nm. Further input parameters are the particle number size distribution and the complex refractive index. Calculations were done by stepwise increasing the real part of the complex refractive index from 1.27 to 1.75 and the imaginary part of the complex refractive index from 0 to 1.8×10^{-2}. The chosen range was supported through literature data of complex refractive indices for aerosol particles.

3.1. Calculation of the complex refractive index

To obtain values of the complex refractive index, the differences between the calculated and measured scattering and absorption efficiencies were minimized. For this purpose, a procedure explained in Wex et al. (2002) was used. The relative difference for the nephelometer scattering (eq. 3) and for the absorption coefficient (eq. 4) are calculated as follows:

$$\Delta_{s,PM_x} = \frac{\sigma^{\mathrm{sim,neph}}_{s,PM_x} - \sigma^{\mathrm{neph}}_{s,PM_x}}{\sigma^{\mathrm{neph}}_{s,PM_x}} \text{ and} \tag{3}$$

$$\Delta_{a,PM_x} = \frac{\sigma^{\mathrm{sim}}_{a,PM_x} - \sigma_{a,PM_x}}{\sigma_{a,PM_x}}, \tag{4}$$

where $\sigma^{\mathrm{neph}}_{s,PM_x}$ and σ_{a,PM_x} are the measured nephelometer scattering and absorption coefficients. $\sigma^{\mathrm{sim,neph}}_{s,PM_x}$ and $\sigma^{\mathrm{sim}}_{a,PM_x}$ are calculated nephelometer scattering and absorption coefficients, calculated from the measured particle number size distribution at the optic rack.

From the entire measurement duration, periods with high dust concentration (Day of Year 2006, 147.1–148.5) and low dust concentration (Day of Year 2006, 149.25–150.5) were used for this purpose. In the following, Day of Year 2006 was abbreviated to DOY. The definition of the different dust concentrations are described at a later stage (Section 4). Figures 2–5 show exemplarily how the refractive index was derived. The nephelometer scattering coefficient at 537 and 637 nm was obtained through interpolation, between the blue and green and the green and red wavelength, respectively. If the iso-lines for 0% relative differences in absorption and scattering have one intersection, an explicit solution of the complex refractive index, containing of a real and an imaginary part is found. If there are potential more crossings of the 0% iso-lines, there is no unambiguous solution. As shown in Figs. 2 and 3, it was not possible to determine an average refractive index during high dust concentration since the relative difference for the nephelometer scattering was apparently minus 34–42% for a wide range of all possible combinations of the refractive index. Furthermore, in Section 4.5 two possible explanations are discussed about the discrepancy of the scattering coefficient during high dust concentration.

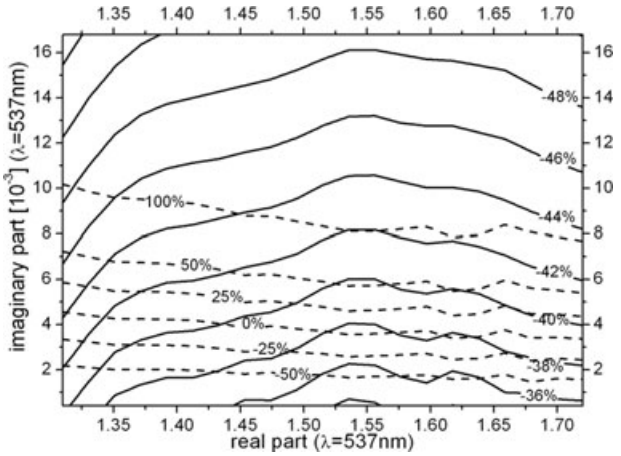

Fig. 2. Average relative differences in percent for nephelometer scattering (solid line) and absorption (dashed line) coefficients at 537 nm for high dust concentration. Lines below and above the dashed zero iso-line indicate the 'worst case uncertainty' for determination of the imaginary part.

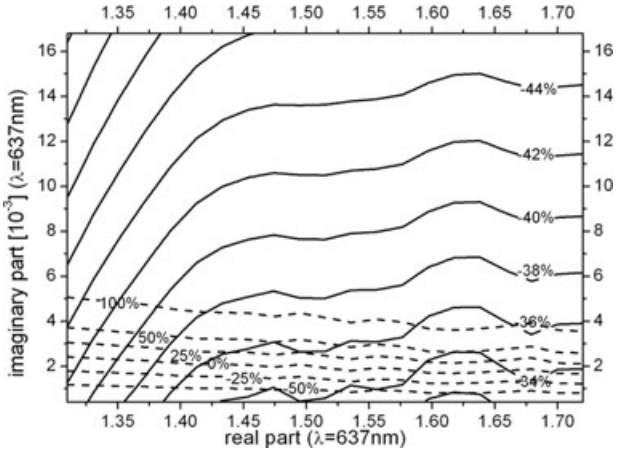

Fig. 3. Average relative differences in percent for nephelometer scattering (solid line) and absorption (dashed line) coefficients at 637 nm for high dust concentration. Lines below and above the dashed zero iso-line indicate the 'worst case uncertainty' for determination of the imaginary part.

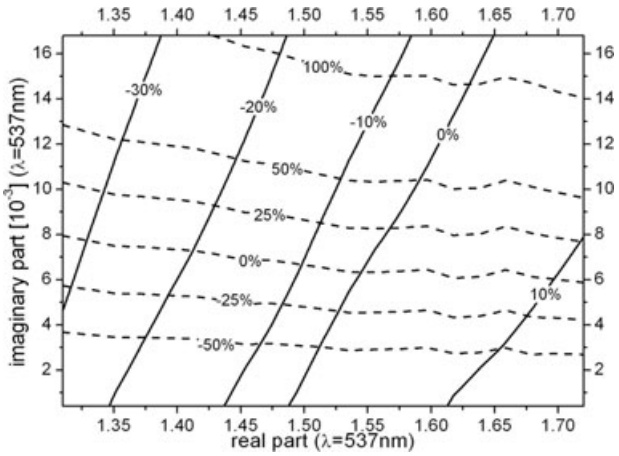

Fig. 4. Average relative differences in percent for nephelometer scattering (solid line) and absorption (dashed line) coefficients at 537 nm for low dust concentration. Lines below and above the dashed zero iso-line indicate the 'worst case uncertainty' for determination of the imaginary part.

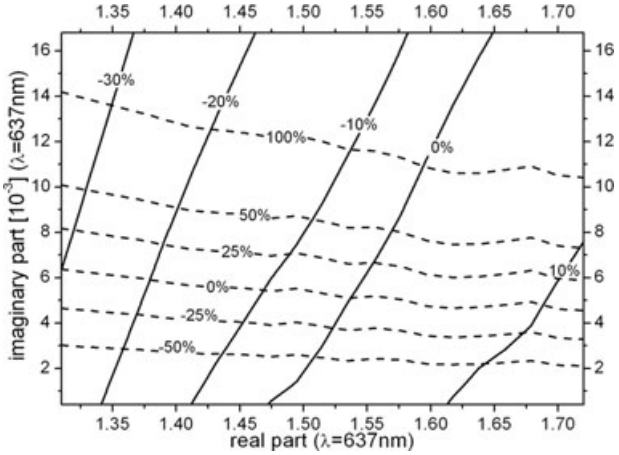

Fig. 5. Average relative differences in percent for nephelometer scattering (solid line) and absorption (dashed line) coefficients at 637 nm for low dust concentration. Lines below and above the dashed zero iso-line indicate the 'worst case uncertainty' for determination of the imaginary part.

Nevertheless, for this case an imaginary part can be estimated, since the imaginary part is not very sensitive with regard to the real part. However, one solution for the refractive index exists for low dust concentration (Figs. 4 and 5).

In the same manner as described above, the imaginary part of the refractive index was calculated for 10 additional time periods, which cover the whole experiment. The real part of the refractive index for low dust concentration was determined from Figs. 4 and 5, and has a value of 1.53 for both wavelengths. Sulphates (e.g. ammonium sulphate) and silicates are predominant particle materials in the submicrometre and supermicrometre size range, respectively (Figs. 10–12). Since both components have similar real parts of the refractive index, a real part of 1.53 was assumed for high dust concentration. This value was also used by Haywood et al. (2003) to calculate radiative properties of dust within the Saharan Dust Experiment (SHADE).

In Fig. 6, the average imaginary parts at 537 and 637 nm for each time period are plotted against the mass-absorption coefficients. For both wavelengths, the mass-absorption coefficient and imaginary part correlate well. A simple parametrization between both quantities was derived. Using a linear relationship between both quantities, the imaginary part was estimated from the mass-absorption coefficient. The mean imaginary parts for

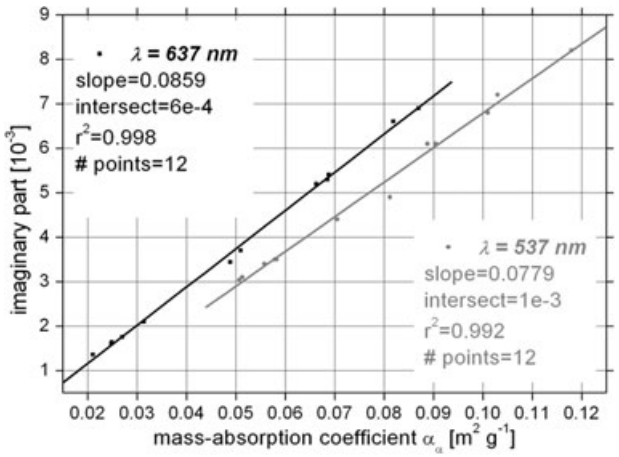

Fig. 6. Average imaginary parts plotted against average mass-absorption coefficients at 537 nm wavelength (grey) and at 637 nm wavelength (black) for 12 sampling periods. Parameters of linear fits and the respective coefficient of determination (r^2) are added.

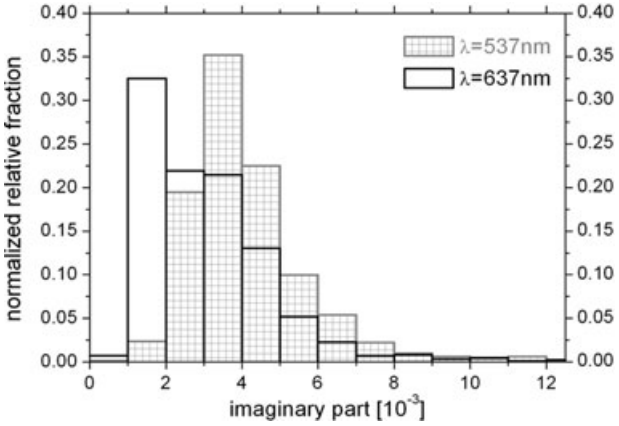

Fig. 7. Histogram of the imaginary parts of the refractive index from DOY 137–158 for 537 and 637 nm. The sum of the normalized relative fractions equals 1.

the entire experiment are 4.1×10^{-3} at 537 nm and 3.1×10^{-3} at 637 nm. A frequency distribution of the imaginary part is illustrated in Fig. 7.

3.2. *Correction of nephelometer scattering, hemispheric backscattering and absorption coefficients to PM$_{10}$*

To calculate the absorption, scattering and hemispheric backscattering coefficients for PM_{10} particles, the following equations are used:

$$\sigma_{a,PM_{10}} = \sigma_{a,PM_x} \cdot \frac{\sigma^{\text{sim}}_{a,PM_{10}}}{\sigma^{\text{sim}}_{a,PM_x}}, \tag{5}$$

$$\sigma_{s,PM_{10}} = \sigma^{\text{neph}}_{s,PM_x} \cdot \frac{\sigma^{\text{sim}}_{s,PM_{10}}}{\sigma^{\text{sim,neph}}_{s,PM_x}}, \tag{6}$$

$$\sigma_{bs,PM_{10}} = \sigma^{\text{neph}}_{bs,PM_x} \cdot \frac{\sigma^{\text{sim}}_{bs,PM_{10}}}{\sigma^{\text{sim,neph}}_{bs,PM_x}}. \tag{7}$$

It was assumed that the refractive indices did not change, when the particle losses to the optic rack were compensated by Mie calculation. The derived refractive indices are used to calculate PM_{10} absorption and scattering coefficients symbolized with the upper Index *sim*. In this calculation, the correction for angular non-idealities (truncation error) as described in Anderson and Ogren (1998) is included. The correction for wavelength Non-idealities is negligible (Anderson and Ogren, 1998) and was left out. The time series of $\sigma_{a,PM_{10}}$ and $\sigma_{s,PM_{10}}$ for both wavelengths are used to calibrate the spectral optical absorption photometer (Müller et al., 2008), which was measuring directly downstream of the inlet without sampling line losses and thus recording PM_{10} particles.

The single scattering albedo and the hemispheric backscatter ratio are calculated as follows:

$$\omega_0 = \frac{\sigma_{s,PM_{10}}}{\sigma_{a,PM_{10}} + \sigma_{s,PM_{10}}} \tag{8}$$

and

$$\beta = \frac{\sigma_{bs,PM_{10}}}{\sigma_{s,PM_{10}}}. \tag{9}$$

Furthermore, the Ångström-scattering-exponent

$$\text{Å}_{\text{sca}}(\lambda_1/\lambda_2) = -\frac{\log(\sigma^{\lambda_1}_{s,PM_{10}}/\sigma^{\lambda_2}_{s,PM_{10}})}{\log(\lambda_1/\lambda_2)}, \tag{10}$$

and the Ångström-absorption-exponent

$$\text{Å}_{\text{abs}}(\lambda_1/\lambda_2) = -\frac{\log(\sigma^{\lambda_1}_{a,PM_{10}}/\sigma^{\lambda_2}_{a,PM_{10}})}{\log(\lambda_1/\lambda_2)}. \tag{11}$$

were calculated for PM_{10} conditions.

3.3. *Derived quantities from the PM$_{10}$ number size distribution*

The effective radius

$$r_{\text{eff}} = \frac{\int r_{ve} \cdot A(r_{ve})}{\int A(r_{ve})} \tag{12}$$

is an often used parameter, which represents the mean radius of the particle surface distribution $A(r_{ve})$. In the following all quantities refer to PM_{10}-conditions and therefore the Index PM_{10} is neglected.

4. Results and discussion

4.1. *Classification of atmospheric dust loadings*

Three different ranges of mineral dust concentrations are discussed for optical properties and the particle number/volume-size distribution of the aerosol in southern Morocco. A measure

for the dust concentration is the total particle number concentration of the dust mode, that appears with a number median diameter around 600 nm.

4.1.1. High dust concentration. During the measurement period from DOY 147 03:00 am to DOY 148 12:00 pm, air masses were advected from desert regions in Algeria and southern Morocco. The wind direction registered at the container roof was mainly northeast with an average velocity of 5.7 m s^{-1}. The average particle number concentration of the dust mode was about 100 particles cm^{-3}.

4.1.2. Low dust concentration. In that period from DOY 149 06:00 am to DOY 150 12:00 pm, the air mass originated over the Atlantic Ocean. The back-trajectories illustrate that the air was transported along the Anti-Atlas mountains to the Tinfou ground station. The prevailing wind direction was southeast with an average velocity of 2.5 m s^{-1}. The average particle number concentration of the dust mode was about 10 particles cm^{-3}.

4.1.3. Medium dust concentration. During DOY 137 12:00 am to DOY 141 03:00 pm, the particle number concentration of the dust mode was in between of low and high dust concentrations. The wind direction was mainly from the east (Fig. 8b) with an average velocity of 3.6 m s^{-1} at 4 m height. Three-dimensional 72-h back-trajectories (Wernli and Davies, 1997) between 950 and 600 hPa ($\sim$0.7 and 4 km above sea level) show air masses transported from the Mediterranean Region over Algeria (Fig. 8c) to the Tinfou ground station. From Lidar observations at Ouarzazate airport, a homogeneous, stable and well mixed boundary layer with a depth between 3–5 km was observed (Tesche et al., 2008). Air parcels from the free troposphere were not mixed in the boundary layer below (Tesche et al., 2008).

4.2. *Optical properties, hygroscopic behaviour, and size distributions for different dust concentrations*

Figure 9a shows a time series of the single scattering albedo (ω_0) for low, medium and high dust concentrations. In general, the single scattering albedo at $\lambda = 537$ nm is lower than at $\lambda = 637$ nm. The imaginary part of the complex refractive index (Fig. 9c) for 537 nm is higher, and therefore, the absorption coefficient is higher for lower wavelengths in the visible spectral range. The highest values of ω_0 are 0.98 ± 0.01 and 0.96 ± 0.02 at 637 and 537 nm wavelength, respectively, occurring during high dust concentration and the imaginary part has the lowest values of all cases. Furthermore, the ratio of the imaginary parts at these two wavelengths is the highest and was explained by dust particles.

The lowest values of ω_0 occurred during low dust concentration. Air masses including background soot (Kaaden et al., 2008) cause up to five times higher imaginary parts of the refractive indices at 637 nm than during high dust concentration (Fig. 9c). Temporarily higher values of the imaginary part (Fig. 9c) with lower values of the single scattering albedo (Fig. 9a) in combination with a smaller effective radius and a higher particle surface concentration (Fig. 9b) can be explained by more externally mixed soot particles in the fine fraction of the particle number size distribution additional to the background soot in the air mass.

Another method for distinguishing dust from other particle material is to determine their hydrophobic nature. Figure 9d shows the number fraction of the hydrophobic particles, which is the highest for high dust concentration for the selected dry diameters: 150, 250 and 350 nm. Only 20% of the 350 nm particles are hygroscopic, that includes the less and more hygroscopic number fraction of particles (Kaaden et al., 2008). For low dust concentration, the number fraction of the hydrophobic constituents is the lowest, especially at 150, 250 and 350 nm.

Figure 8 illustrates the average particle number and volume size distributions for each period. For the particle volume-size distribution, the dust mode is clearly dominant and has a volume median diameter around 2–3 μm. During a sandstorm event, other than that mentioned periods, the particle number concentration of the dust mode reached 1000 particles cm^{-3}. For all periods the particle number concentration of the accumulation mode for the number size and volume size distribution shows only small variation with a median diameter around 70–90 nm and a volume median diameter of about 300 nm.

4.3. *Comparison of single particle analysis results with optical properties and measured size distributions*

A size - resolved single particle analysis of aerosol particles collected at Tinfou was performed using scanning electron microscopy with energy-dispersive X-ray analysis. Results from these analysis are shown in Figs. 10–12 for the three selected periods. In general, from a mineralogical view, a bimodal distribution prevailed for the main components sulphate and mineral dust. From 200 to 500 nm sulphate particles are abundant, whose overwhelming majority were specified as ammonium sulphate particles (Kandler et al., 2008). Particles larger than 500 nm predominantly consist of silicates, quartz and calcium carbonates. Light absorbing iron-containing particles were found in the particle size range from 200 nm to 10 μm. However, a comparison of the periods revealed that the fraction of the total iron-containing particles for high dust concentration is 71% higher than for low dust concentration and 40% higher than for medium dust concentration.

For the accumulation mode, sulphate is the predominant particle material, whereas for the dust mode it is silicate. If the dust mode has a low particle number concentration, the relative fraction of sulphates from the accumulation mode in the particle diameter range between 500 nm and 2.5 μm is enhanced. In opposite of that, when the particle number size distribution in the dust mode is higher, the sulphate fraction between 500 nm and 2.5 μm is reduced. It is concluded that the Saharan aerosol

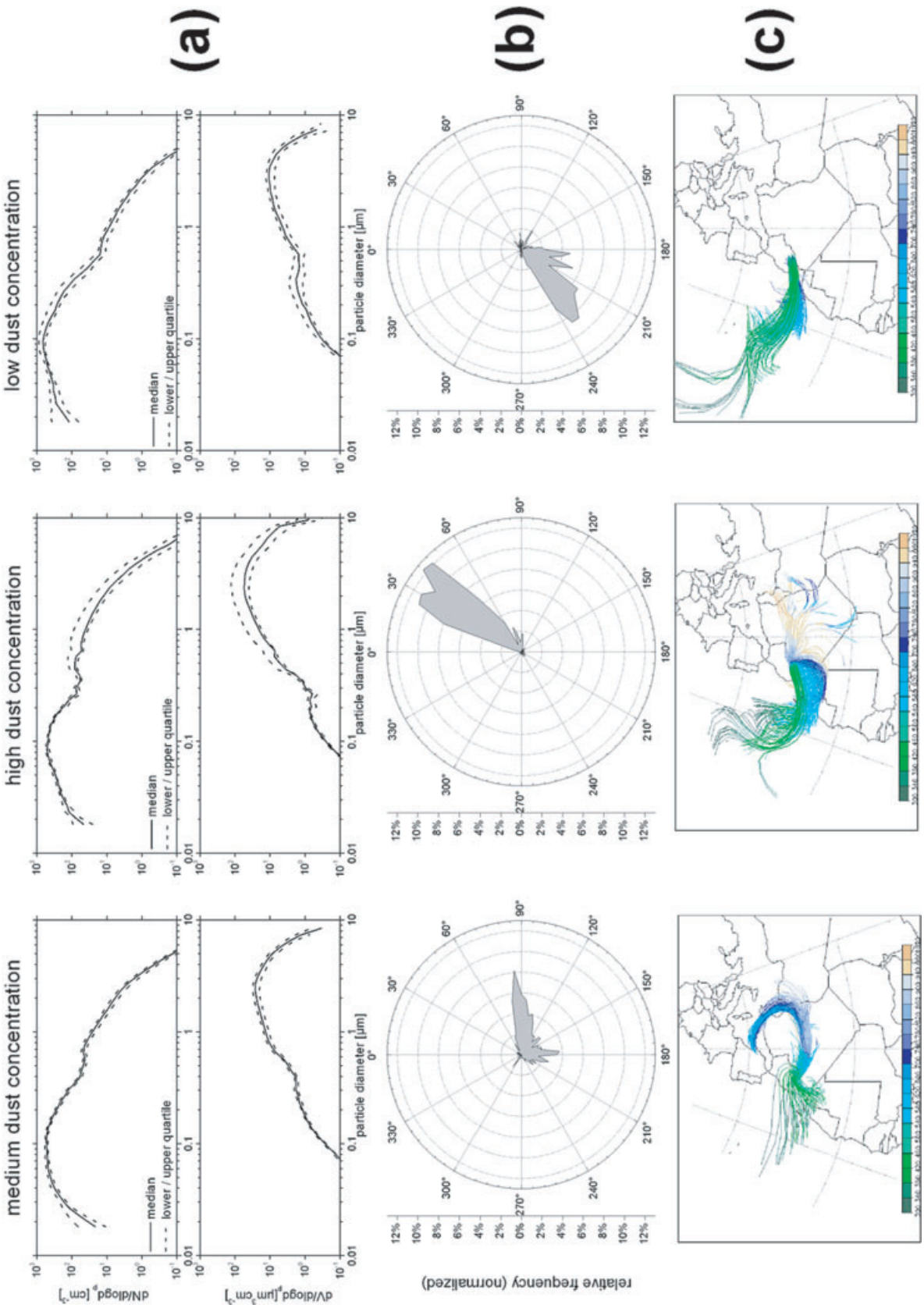

Fig. 8. (a) Median (solid line) and lower/upper quartiles (dashed line) of the number and volume particle size distributions, (b) wind distribution at the Tinfou ground station and (c) 72-h back-trajectories for medium dust concentration (DOY 137–141.63), high dust concentration (DOY 147.1–148.5) and low dust concentration (DOY 149.25–150.5).

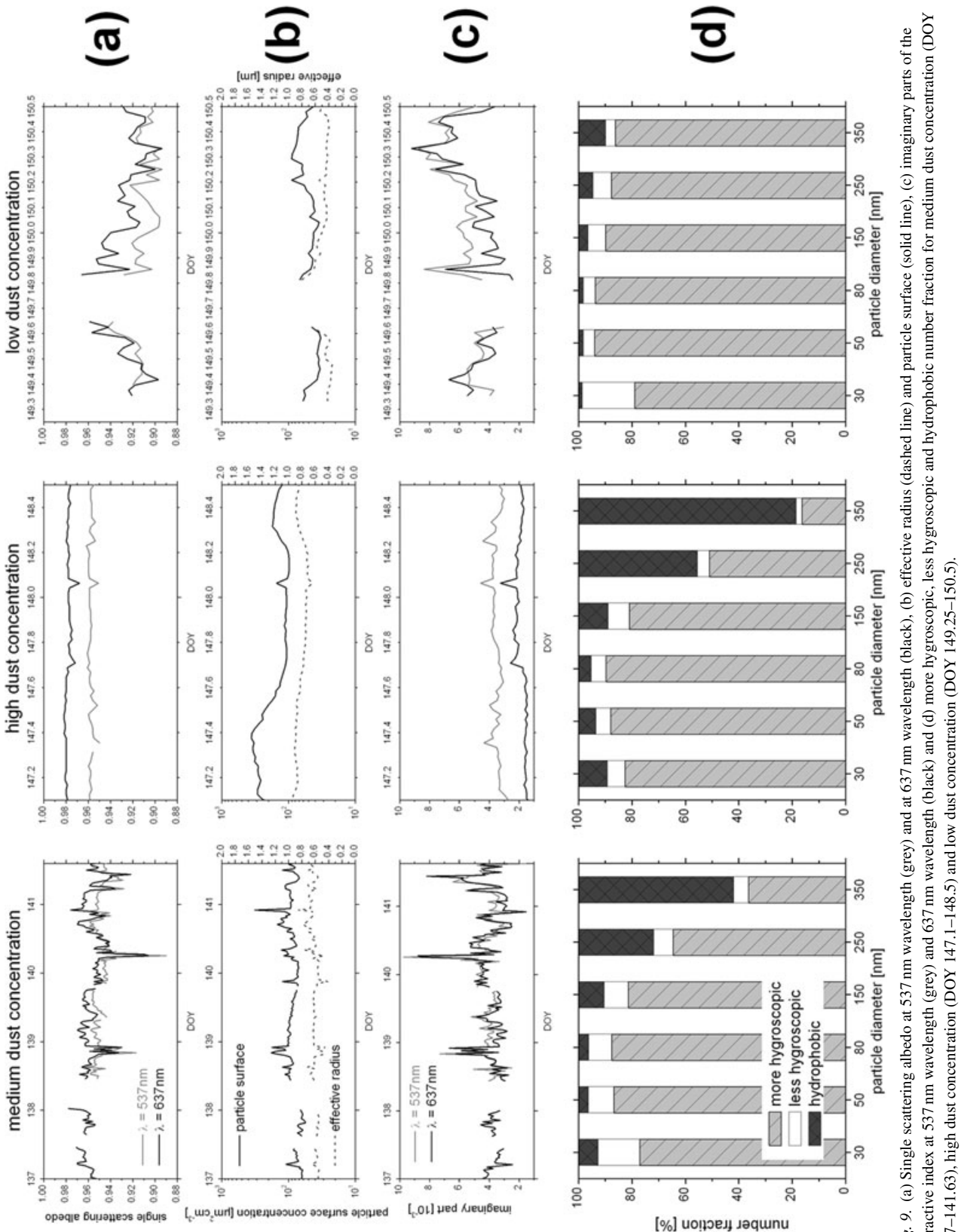

Fig. 9. (a) Single scattering albedo at 537 nm wavelength (grey) and at 637 nm wavelength (black), (b) effective radius (dashed line) and particle surface (solid line), (c) imaginary parts of the refractive index at 537 nm wavelength (grey) and 637 nm wavelength (black) and (d) more hygroscopic, less hygroscopic and hydrophobic number fraction for medium dust concentration (DOY 137–141.63), high dust concentration (DOY 147.1–148.5) and low dust concentration (DOY 149.25–150.5).

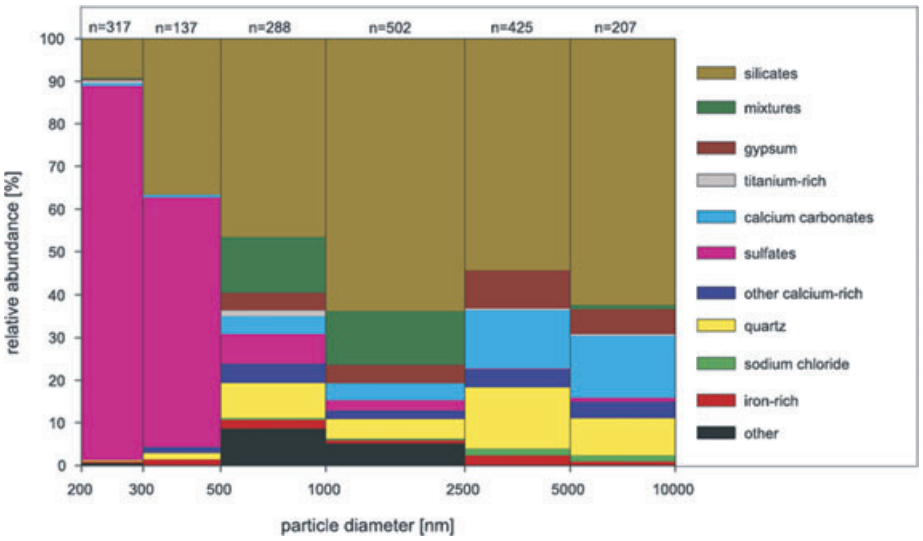

Fig. 10. Chemical composition of aerosol particles from single particle analysis for 19 May 11:27–11:42 assigned to medium dust concentration; n denotes the number of particles in each column, that were analysed.

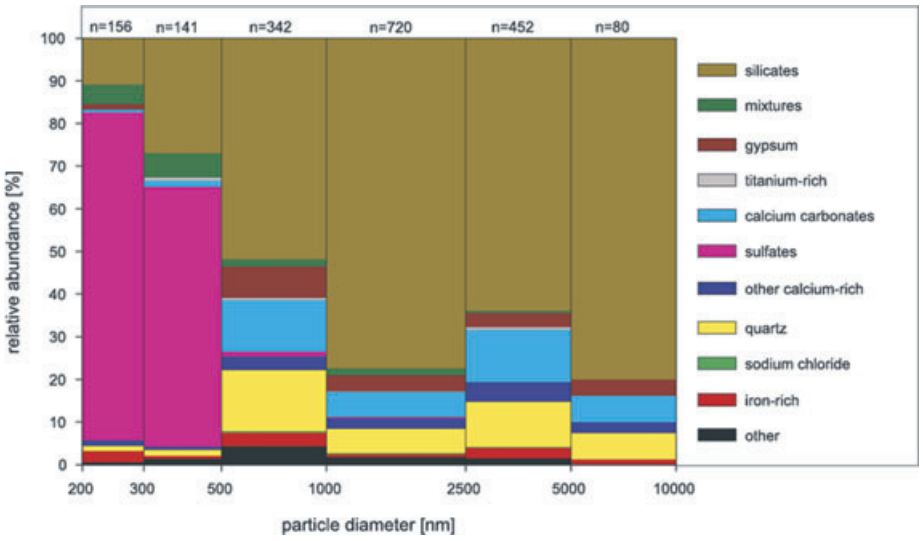

Fig. 11. Chemical composition of aerosol particles from single particle analysis for 27 May 10:56-11:08 assigned to high dust concentration; n denotes the number of particles in each column, that were analysed.

at Tinfou between 200 nm and 10 μm is a two main component mixture of sulphate and mineral dust.

4.4. *Optical properties with regard to the effective radius and comparison with other results*

Table 2 lists the optical parameters of 12 time periods according to their average effective radius. The three time periods, which were discussed in detail above, are included in this table. The larger the effective radius, the more the particle population is dominated by the dust mode.

The backscatter ratio (β) and the imaginary part of the complex refractive index decrease with increasing effective radius for both investigated wavelengths. The former change was shown in Heintzenberg (1978). If mineral dust particles dominate the particle population, the single scattering albedo is the highest for both wavelengths. The single scattering albedo is the lowest when the influence of soot particles becomes more important.

At $\lambda = 637$ nm, the single scattering albedo of about 0.98 ± 0.01 is comparable with the value of 0.97 ± 0.01 given by Alfaro et al. (2004) from a Tunisian soil-sample. Sun-photometer measurements during the SHADE field campaign, which took place at the Cape Verde Islands, yielded values for ω_0 of about 0.96 and 0.97 for 440 nm and 673 nm (Haywood et al., 2003), respectively. From aircraft measurements near that site using a PSAP and a TSI integrating nephelometer, ω_0-values around

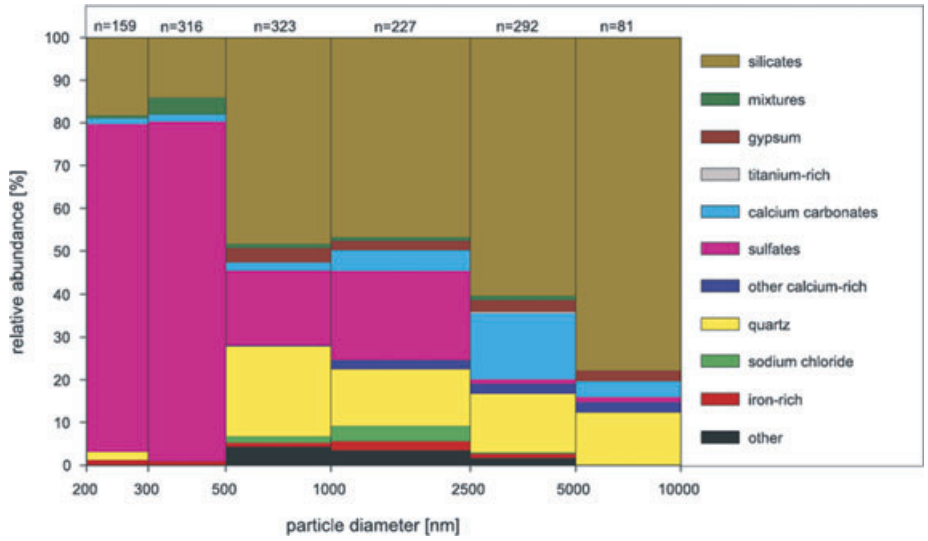

Fig. 12. Chemical composition of aerosol particles from single particle analysis for 30 May 8:43–8:53 assigned to low dust concentration; n denotes the number of particles in each column, that were analysed.

0.97 ± 0.02 at $\lambda = 550$ nm were derived (Haywood et al., 2003). All these data confirm our results. Linke et al. (2006) reported an ω_0 value of 0.980 ± 0.002 around 530 nm, which is higher than 0.96 ± 0.02 at the Tinfou ground station. Linke et al. (2006) however measured the absorption coefficient of pure dust particles in a laboratory with a photo-acoustic absorption spectrometer (PAS) downstream of an impactor with a cut-off diameter of 1.2 μm, which differs from our measurement design.

The Ångström-absorption-exponent characterizes the absorption spectrum (see eq. 11). Whereas soot particles show a slight decrease of the absorption coefficient ($\sigma_a(\lambda) \sim \lambda^{-1}$) with increasing wavelength (Horvath, 1993), the absorption of hematite rapidly decreases in the visible spectral range.

An Ångström-absorption-exponent around 1 for smaller effective radii reveals a stronger influence of soot particles. Aerosol from high - temperature processes with black carbon as a dominant absorbing component has a Ångström-absorption-exponent around 1 (Kirchstetter et al., 2004). Measurements by Linke et al. (2006) denote an Ångström-absorption-exponent of 4.2 for a Morocco soil-sample between 266 and 532 nm. The measurements of this study offer a similar value for high dust concentration of approximately 4 to 5, but for the wavelengths 537 and 637 nm. Hence, iron-containing particles are the main absorber in the mineral dust mode. Furthermore, during high dust concentration the iron-containing particle fraction from electron microscopy of single particles (Kandler et al., 2008), is higher than in the other periods.

Additional information with regard to the absorbing material can be derived from a comparison of the average wind speed and the Ångström-absorption-exponent. The highest values occurred during high wind speeds. This evidence is caused by the saltation mechanism, lifting the crust material including iron oxide into the air. In contrast of that, if the wind speed is low, the Ångström-absorption-exponent is low, too. In these cases the imaginary parts of the refractive index are little higher.

The Ångström-scattering-exponent in this investigation is around zero and sometimes negative for larger effective radii, which corresponds with the findings in Alfaro et al. (2004).

4.5. *Effect of particle shape on scattering coefficients and nephelometer uncertainty for supermicrometre particles*

Differences of scattering properties for non-spherical particles were discussed by Mishchenko et al. (1997), Kalashnikova and Sokolik (2002) and Kalashnikova et al. (2005). Mishchenko et al. (2000) point out that there are differences between measured and Mie-calculated scattering properties for mineral dust particles. One measure of particle irregularity is the dynamic shape factor, which increases with particle size (Okada et al., 2001; Kalashnikova et al., 2005). Reasons for the discrepancy between measured and calculated scattering coefficients during high dust concentration, which exhibited a high number of large non-spherical dust particles, are illustrated below.

Kalashnikova et al. (2005) presented different types of dust, different size distributions for spheres, grains, plates and oblate/prolate spheroids together with scattering phase functions at $\lambda = 550$, 672 and 866 nm. For the present investigation grain-like and weakly absorbing particles with imaginary parts of the refractive index of 2.1×10^{-3}, 1.1×10^{-3} and 7.0×10^{-4} were used. Kalashnikova et al. (2005) point out that these particles describe the Saharan dust plume well. A combined discrete dipole approximation (DDA) and T-Matrix model were used by Kalashnikova et al. (2005) to calculate the single scattering

Table 2. Average wind velocity at the Tinfou ground station, imaginary part(λ) of the refractive index, backscatter ratio(λ), single scattering albedo(λ), Ångström-absorption-exponent (λ_1/λ_2), Ångström-scattering-exponent (λ_1/λ_2), more hygroscopic/hydrophobic number fraction at 30, 80, 150 and 350 nm for 12 sampling periods according to the effective radius. In parentheses: uncertainties described in Section 2.2

$r_{\text{eff}}(\mu\text{m})$	Period [DOY]	$\overline{v}[\frac{m}{s}]$	n(537 nm)	n(637 nm)	β(550 nm)	ω_0(537 nm)	ω_0(637 nm)	$\text{Å}_{abs}(\frac{537}{637})$	$\text{Å}_{sca}(\frac{450}{550})$	nf_{30}^{hyg}	nf_{80}^{hyg}	nf_{150}^{hyg}	nf_{350}^{hyg}
			u(n)	u(n)	u(β)	u(ω_0)	u(ω_0)			nf_{30}^{hyd}	nf_{80}^{hyd}	nf_{150}^{hyd}	nf_{350}^{hyd}
0.439	152.146-152.25	5.3	$8.45{\cdot}10^{-3}$	$5.49{\cdot}10^{-3}$	0.13	0.89	0.93	2.97	0.39	0.46	0.84	0.74	0.74
										0.34	0.10	0.08	0.21
			($3.38{\cdot}10^{-3}$)	($1.23{\cdot}10^{-3}$)	(0.02)	(0.02)	(0.01)						
0.475	151.06-151.375	2.1	$7.22{\cdot}10^{-3}$	$6.69{\cdot}10^{-3}$	0.11	0.91	0.92	1.10	0.59	0.50	0.78	0.87	0.74
										0.06	0.16	0.09	0.24
			($2.89{\cdot}10^{-3}$)	($1.51{\cdot}10^{-3}$)	(0.02)	(0.02)	(0.01)						
0.484	149.25-150.5	3.0	$5.70{\cdot}10^{-3}$	$4.93{\cdot}10^{-3}$	0.12	0.91	0.93	1.72	0.54	0.79	0.94	0.90	0.86
										0.01	0.02	0.04	0.10
			($2.28{\cdot}10^{-3}$)	($1.11{\cdot}10^{-3}$)	(0.02)	(0.02)	(0.01)						
0.507	146-146.396	6.3	$5.34{\cdot}10^{-3}$	$3.70{\cdot}10^{-3}$	0.12	0.93	0.96	2.78	0.05	0.73	0.84	0.86	0.38
										0.16	0.06	0.06	0.58
			($2.14{\cdot}10^{-3}$)	($8.33{\cdot}10^{-4}$)	(0.02)	(0.02)	(0.01)						
0.516	143-143.3	1.6	$6.61{\cdot}10^{-3}$	$6.71{\cdot}10^{-3}$	0.10	0.93	0.93	1.03	0.27	0.76	0.83	0.68	0.55
										0.15	0.02	0.13	0.39
			($2.65{\cdot}10^{-3}$)	($1.51{\cdot}10^{-3}$)	(0.01)	(0.02)	(0.01)						
0.615	137-141.625	3.6	$4.21{\cdot}10^{-3}$	$3.94{\cdot}10^{-3}$	0.09	0.95	0.96	1.24	0.14	0.77	0.88	0.81	0.36
										0.07	0.04	0.10	0.58
			($1.68{\cdot}10^{-3}$)	($8.87{\cdot}10^{-4}$)	(0.01)	(0.02)	(0.01)						
0.642	148.75-148.875	1.4	$5.86{\cdot}10^{-3}$	$5.05{\cdot}10^{-3}$	0.10	0.94	0.95	1.59	-0.10	0.92	0.95	0.79	0.37
										0.06	0.02	0.14	0.58
			($2.34{\cdot}10^{-3}$)	($1.14{\cdot}10^{-3}$)	(0.01)	(0.02)	(0.01)						
0.706	155-158	3.5	$3.45{\cdot}10^{-3}$	$2.26{\cdot}10^{-3}$	0.10	0.95	0.97	3.14	0.06	0.74	0.90	0.85	0.26
										0.07	0.04	0.08	0.70
			($1.73{\cdot}10^{-3}$)	($5.65{\cdot}10^{-4}$)	(0.01)	(0.02)	(0.01)						
0.817	147.125-148.5	5.7	$3.56{\cdot}10^{-3}$	$1.88{\cdot}10^{-3}$	0.10	0.96	0.98	4.06	-0.12	0.83	0.90	0.81	0.16
										0.11	0.05	0.11	0.81
			($1.78{\cdot}10^{-3}$)	($4.70{\cdot}10^{-4}$)	(0.01)	(0.02)	(0.01)						
0.863	150.52-151.02	5.6	$2.96{\cdot}10^{-3}$	$1.68{\cdot}10^{-3}$	0.09	0.95	0.97	3.74	0.00	0.56	0.93	0.86	0.10
										0.09	0.02	0.06	0.88
			($1.48{\cdot}10^{-3}$)	($4.20{\cdot}10^{-4}$)	(0.01)	(0.02)	(0.01)						
0.894	147.1-147.458	8.2	$3.46{\cdot}10^{-3}$	$1.57{\cdot}10^{-3}$	0.09	0.96	0.98	4.67	-0.14	0.84	0.89	0.74	0.09
										0.09	0.05	0.17	0.90
			($1.73{\cdot}10^{-3}$)	($3.93{\cdot}10^{-4}$)	(0.01)	(0.02)	(0.01)						
0.960	145-145.458	12.6	$2.89{\cdot}10^{-3}$	$1.27{\cdot}10^{-3}$	0.09	0.96	0.98	4.73	-0.05	0.97	0.94	0.82	N.A.
										0.03	0.01	0.14	N.A.
			($1.44{\cdot}10^{-3}$)	($3.18{\cdot}10^{-4}$)	(0.01)	(0.02)	(0.01)						

albedo ω_0 and the normalized extinction coefficients K_e for a monomodal size distribution with a number median diameter of 1 μm and a geometric standard deviation of 1.5. This kind of size distribution represents the measured dust size distribution at the Tinfou ground station.

To calculate the discrepancy between the nephelometer scattering coefficient for the grain like and the spherical particle size distribution, the scattering phase functions at 550, 672 and 866 nm wavelength was needed. The degree of the discrepancy in scattering defined by the relative difference:

$$\Delta_s = \frac{\Sigma_{\sin\theta}^{\text{grains}} \cdot \Sigma_{F\theta}^{\text{spheres}}}{\Sigma_{F\theta}^{\text{grains}} \cdot \Sigma_{\sin\theta}^{\text{spheres}}} \cdot \frac{\sigma_s^{\text{spheres}}}{\sigma_s^{\text{grains}}} - 1 \tag{13}$$

and for absorption:

$$\Delta_a = \frac{\sigma_a^{\text{spheres}}}{\sigma_a^{\text{grains}}} - 1, \tag{14}$$

where

$$\Sigma_{\sin\theta}^{\text{grains}} = \int_0^{\pi} p(\lambda, \widetilde{m}, \theta)^{\text{grains}} \sin(\theta) \mathrm{d}\theta, \tag{15}$$

$$\Sigma_{F\theta}^{\text{grains}} = \int_0^{\pi} p(\lambda, \widetilde{m}, \theta)^{\text{grains}} F(\theta) \mathrm{d}\theta, \tag{16}$$

$$\Sigma_{\sin\theta}^{\text{spheres}} = \int_0^{\pi} p(\lambda, \widetilde{m}, \theta)^{\text{spheres}} \sin(\theta) \mathrm{d}\theta \text{and} \tag{17}$$

$$\Sigma_{F\theta}^{\text{spheres}} = \int_0^{\pi} p(\lambda, \widetilde{m}, \theta)^{\text{spheres}} F(\theta) \mathrm{d}\theta, \tag{18}$$

where σ_s^{grains}, $\sigma_s^{\text{spheres}}$, σ_a^{grains} and $\sigma_a^{\text{spheres}}$ are the normalized scattering and absorption coefficients. The latter were derived from ω_0 and K_e for each wavelength. $F(\theta)$ is the angular response function of the TSI nephelometer (Anderson et al., 1996) and $p(\lambda, \widetilde{m}, \theta)$ the scattering phase function of the spheres and grains (Kalashnikova et al., 2005). Table 3 shows the relative differences for the nephelometer scattering and absorption coefficients. The relative difference for nephelometer scattering coefficients is higher at lower wavelengths. No statements can be made about the wavelength dependence of the relative difference of the absorption coefficient (Table 3). Figures 2 and 3 show a comparable wavelength dependence for scattering, but with higher relative differences (around −40% at 537 nm and −35% at 637 nm). We conclude that the discrepancy between measured and calculated nephelometer scattering coefficient can be explained by the non-sphericity of larger particles.

Table 3. Relative differences of nephelometer scattering (Δ_s) and absorption coefficients (Δ_a) for spherical and non-spherical (grain-like) weakly absorbing particles

λ (nm)	Δ_s	Δ_a
550	−15.5%	1.83%
672	−9.24%	2.56%
866	−2.1%	−6%

An additional explanation for the discrepancy might be caused through higher measurement uncertainties for supermicrometre particles. In an intercomparison workshop Heintzenberg et al. (2006) compared nine TSI Nephelometers (model 3563) with each other using DEHS[1] test particles. All tested TSI integrating nephelometer differed about 13% for the total green wavelength. This value is significantly higher than the unit to unit uncertainty of about 7%, used in former publications (e.g. Wex et al., 2002).

5. Summary and conclusion

In this paper, in situ measurements of optical and physical properties of mineral dust particles were investigated for a source region of the Saharan Desert. The presented measurements were performed under stable thermodynamic conditions in an air-conditioned container. Results presented in this investigation are valid for PM_{10} conditions. Concerning the size and morphology of mineral dust particles, size depended dry dynamic shape factors for the submicrometre and the supermicrometre range were used. They ranged from 1.0 for particles up to 550 nm volume equivalent diameter to 1.26 for super-micrometer particles with a dust particle density of 2.7 g cm^{-3}. Results of sub-micrometer size distributions from a Differential Mobility Particle Sizer were corrected for multiply charged particles using data from APS measurements. Supermicrometre particles, carrying a lot of multiply charged particles influence the standard charge inversion routine, if they were not removed physically.

A further data correction in addition to Bond et al. (1999) was used for particulate absorption measurements with a PSAP. The new correction was required, because the particle loading on the filter influences the measured absorption coefficients.

As a main part of our results, we distinguish between three distinct levels of dust concentrations, selected from the entire measurement period. Low and high dust concentrations representing two extremes with respect to dust fraction and single scattering albedo. During high dust concentration, the dust mode appears with a number median diameter around 600 nm. This level had a 10 times higher particle number concentration (100 particles cm^{-3}) comparing with low dust concentration. During high dust concentration, the values of the single scattering albedo have been 0.96 ± 0.02 and 0.98 ± 0.01 at 537 and 637 nm, respectively. These values are significantly higher than during low dust concentration with 0.89 ± 0.02 and 0.93 ± 0.01 for the same wavelengths. The average complex refractive indexes from the entire period as derived from calculated and measured absorption and scattering coefficients are 1.53–4.1 × 10^{-3} i and 1.53–3.1 × 10^{-3} i at 537 and 637 nm wavelength, respectively. Since the real part of the complex refractive

[1] di-ethyl-hexyl-sebacate

index was constant with time, the imaginary part was highly variable depending on the extend of the dust mode. As a result from the comparison of the spectral behaviour of the absorption coefficient, the main absorber in the dust mode is iron oxide, whereas the absorption for smaller particles ($dp_{ve} < 300$ nm) can be explained by soot-type particles. During high dust concentration with large effective radius and low imaginary part, the particulate absorption is more influenced by iron oxide, having a lower imaginary part than soot at 537 and 637 nm wavelength. During low dust concentration and higher absorption, the imaginary part is more influenced by a soot-type absorber, with a higher imaginary part than iron oxide at the investigated wavelengths. The main mineralogical and non-absorbing components are sulphate in the accumulation mode and silicate in the dust mode.

Discrepancies between calculated and measured scattering coefficients during high dust concentration could be caused by the higher fraction of non-spherical particles.

The results of the presented study are important when comparing e.g. radiances, observed with the Multi-angle Imaging SpectroRadiometer (MISR). They can also serve as input parameter, for example, for the dust model system LM-MUSCAT-DES (Heinold et al., 2007, 2008) and may be used in modelling the MISR satellite response. The results of this investigation about optical and physical properties of dust particles at a source region are specifically important to identify and compare data with studies such as the SAMUM-2 field campaign (Cape Verde Islands, January/February 2008).

6. Acknowledgments

The present study was supported in part by the German Research Foundation (project FOR 539) within the Research Group SAMUM. We acknowledge Peter Knippertz from the Johannes Gutenberg-University of Mainz for preparing the figures of the back-trajectories. Also we acknowledge Matthias Tesche from the Leibniz Institute for Tropospheric Research, who advises us on the structure of the dusty boundary layer.

References

Alfaro, S. C., Lafon, S., Rajot, J. L., Formenti, P., Gaudichet, A. and co-authors. 2004. Iron oxides and light absorption by pure desert dust: an experimental study. *J. Geophys. Res.* **109**, D08208, doi:10.1029/2003JD04374.

Anderson, T. L. and Ogren, J. A. 1998. Determining aerosol radiative properties using the TSI 3563 integrating nephelometer. *Aerosol Sci. Technol.* **29**, 57–69.

Anderson, T. L., Covert, D. S., Marshall, S. F., Laucks, M. L., Charlson, R. J. and co-authors. 1996. Performance characteristics of a high-sensitivity, three-wavelength, total scatter/backscatter nephelometer. *J. Atmos. Oceanic Technol.* **13**, 967–986.

Balkanski, Y., Schulz, M., Claquin, T. and Guibert, S. 2007. Reevaluation of mineral aerosol radiative forcings suggests a better agreement with satellite and AERONET data. *Atmos. Chem. Phys.* **7**, 81–95.

Bedidi, A. and Cervelle, B. 1993. Light scattering by spherical particles with hematite and goethitelike optical properties—effect of water impregnation. *J. Geophys. Res.* **98**, 11 941–11 951.

Birmili, W., Stratmann, F. and Wiedensohler, A. 1999. Design of a DMA-based size spectrometer for a large particle size range and stable operation. *J. Aerosol Sci.* **30**, 549–553.

Bohren, C. F. and Huffman, D. R. 1983. *Absorption and Scattering of Light by Small Particles*. John Wiley & Sons, Inc, New York.

Bond, T. C. Anderson, T. L. and Campbell, D. 1999. Calibration and intercomparison of filter-based measurements of visible light absorption by aerosols. *Aerosol Sci. Technol.* **30**, 582–600.

Brockmann, J. E. 1993. Sampling and Transport of Aerosols. In: *Aerosol Measurement—Principles, Techniques, and Applications*. Van Nostrand Reinhold, New York, 77–108.

Decarlo, P., Slowik, J., Worsnop, D., Davidovits, P. and Jimenez, J. 2004. Particle morphology and density characterization by combined mobility and aerodynamic diameter measurements. Part 1: theory. *Aerosol Sci. Technol.* **38**, 1185–1205.

Engelstaedter, S., Tegen, I. and Washington, R. 2006. North African dust emissions and transport. *Earth-Sci. Rev.* **79**, 73–100.

Goudie, A. S. and Middleton, N. J. 2001. Saharan dust storms: nature and consequences. *Earth-Sci. Rev.* **56**, 179–204.

Haywood, J. M., Francis, P. N., Glew, M. D. and Taylor, J. P. 2001. Optical properties and direct radiative effect of Saharan dust—a case study of two Saharan dust outbreaks using aircraft data. *J. Geophys. Res.* **106**, 18 417–18 430.

Haywood, J., Francis, P., Osborne, S., Glew, M., Loeb, N. and co-authors. 2003. Radiative properties and direct radiative effect of Saharan dust measured by the C-130 aircraft during SHADE: 1. Solar spectrum. *J. Geophys. Res.* **108**, (D18), 8577, doi:10.1029/2002JD002687.

Heinold, B., Helmert, J., Hellmuth, O., Wolke, R., Ansmann, A. and co-authors. 2007. Regional modeling of Saharan dust events using LM-MUSCAT: model description and case studies. *J. Geophys. Res.-all series* **112**, 11204, doi:10.1029/2006jd007443.

Heinold, B., Tegen, I., Esselborn, M., Kandler, K., Knippertz, P. and co-authors. 2008. Regional Saharan Dust Modelling during the SAMUM 2006 Campaign. *Tellus* **61B**, doi:10.1111/j.1600-0889.2008.00387.x.

Heintzenberg, J. 1978. The angular calibration of the total scatter/backscatter nephelometer, consequences and applications. *Staub-Reinhaltl. Luft* **38**, 62–63.

Heintzenberg, J. and Quenzel, H. 1973. On the effect of the loss of large particles on the determination of scattering coefficients with integrating nephelometers. *Atmos. Environ.* **7**, 503–507.

Heintzenberg, J., Müller, K., Birmili, W., Spindler, G. and Wiedensohler, A. 1998. Mass-related aerosol properties over the Leipzig basin. *J. Geophys. Res.* **103**, 13 125–13 136.

Heintzenberg, J., Wiedensohler, A., Tuch, T. M., Covert, D. S., Sheridan, P. and co-authors. 2006. Intercomparisons and aerosol calibrations of 12 commercial integrating nephelometers of three manufacturers. *J. Atmos. Oceanic Technol.* **23**, 902–914.

Hinds, W. C. 1999. *Aerosol Technology: Properties, Behavior, and Measurement of Airborne Particles*. John Wiley & Sons, Inc, New York.

Horvath, H. 1993. Atmospheric light absorption- a review. *Atmos. Environ.* **27A**, 293–317.

Hsu, W. and Matijevic, E. 1985. Optical properties of monodispersed hematite hydrosols. *Appl. Opt.* **24**, 1623–1637.

Jokinen, V. and Mäkelä, J. M. 1997. Closed-loop arrangement with critical orifice for DMA sheath/excess flow system. *J. Aerosol Sci.* **28**, 643–648.

Kaaden, N., Massling, A., Schladitz, A., Müller, T., Kandler, K. and co-authors. 2008. State of mixing, shape factor, number size distribution, and hygroscopic growth of the saharan anthropogenic and mineral dust aerosol at Tinfou, Morocco. *Tellus* **61B**, doi:10.1111/j.1600-0899.2008.00388.x.

Kalashnikova, O. V. and Sokolik, I. N. 2002. Importance of shapes and compositions of wind-blown dust particles for remote sensing at solar wavelengths. *Geophys. Res. Lett.* **29**, 38–31.

Kalashnikova, O. V., Kahn, R., Sokolik, I. N. and Li, W. H. 2005. Ability of multiangle remote sensing observations to identify and distinguish mineral dust types: 1. Optical models and retrievals of optically thick plumes. *J. Geophys. Res.* **110**, D18514, doi:10.1029/2004JD004550.

Kandler, K., Deutscher, C., Ebert, M., Hofmann, H., Jäckel, S. and co-authors. 2008. Size distribution, mass concentration, chemical and mineral composition, and derived optical parameters of the boundary layer aerosol at Tinfou, Morocco, during SAMUM 2006. *Tellus* **61B**, doi:10.1111/j.1600-0899.2008.00385.x.

Kaufman, Y. J., Tanré, D. and Boucher, O. 2002. A satellite view of aerosols in the climate system. *Nature* **419**, 215–223.

Kaufman, Y. J., Koren, I., Remer, L. A., Tanré, D., Ginoux, P. and co-authors. 2005. Dust transport and deposition observed from the terra-moderate resolution imaging spectroradiometer (modis) spacecraft over the atlantic ocean. *J. Geophys. Res.* **110**, D10512, doi:10.1029/2003JD004436.

Kirchstetter, T. W., Novakov, T. and Hobbs, P. V. 2004. Evidence that the spectral dependence of light absorption by aerosols is affected by organic carbon. *J. Geophys. Res.* **109**, D21208, doi:10.1029/2004JD0049999.

Lafon, S., Rajot, J. L., Alfaro, S. C. and Gaudichet, A. 2004. Quantification of iron oxides in desert aerosol. *Atmos. Environ.* **38**, 1211–1218.

Leinert, S. and Wiedensohler, A. 2008. A DMA and APS based technique for measuring aerodynamic hygroscopic growth factors of micrometer-size aerosol particles. *J. Aerosol Sci.* **39**, 393–402.

Liao, H. and Seinfeld, J. H. 1998. Radiative forcing by mineral dust aerosols—sensitivity to key variables. *J. Geophys. Res.* **103**, 31 637–31 646.

Linke, C., Möhler, O., Veres, A., Mohácsi, Á., Bozóki, Z. and co-authors. 2006. Optical properties and mineralogical composition of different Saharan mineral dust samples: a laboratory study. *Atmos. Chem. Phys.* **6**, 3315–3323.

Luo, C., Mahowald, N. M. and Del Corral, J. 2003. Sensitivity study of meteorological parameters on mineral aerosol mobilization, transport, and distribution. *J. Geophys. Res.* **108**, (D15), 4447, doi:10.1029/2003JD003483.

Mishchenko, M. I., Travis, L. D., Kahn, R. A. and West, R. A. 1997. Modeling phase functions for dustlike tropospheric aerosols using a shape mixture of randomly oriented polydisperse spheroids. *J. Geophys. Res.* **102**, (D14), 16831–16847.

Mishchenko, M. I., Wiscombe, W. J., Hovenir, J. W. and Travis, L. D. 2000. Overview of Scattering by Nonspherical Particles In: *Light Scattering by Nonspherical Particles*. Academic Press, San Diego, 30–59.

Müller, T., Schladitz, A., Massling, A., Kaaden, N., Kandler, K. and co-authors. 2008. Spectral absorption coefficients and imaginary parts of refractive indices of Saharan dust during SAMUM-1. *Tellus* **61B**, doi:10.1111/j.1600-0889.2008.00399.x.

Okada, K., Heintzenberg, J., Kai, K. and Qin, Y. 2001. Shape of atmospheric mineral particles collected in three Chinese arid-regions. *Geophys. Res. Lett.* **28**, 3123–3126.

Petzold, A. and Schönlinner, M. 2004. Multi-angle absorption photometry: a new method for the measurement of aerosol light absorption and atmospheric black carbon. *J. Aerosol Sci.* **35**, 421–441.

Petzold, A., Schloesser, H., Sheridan, P. J., Arnott, W. P., Ogren, J. A. and co-authors. 2005. Evaluation of multiangle absorption photometry for measuring aerosol light absorption. *Aerosol Sci. Technol.* **39**, 40–51.

Petzold, A., Rasp, K., Weinzierl, B., Esselborn, M., Hamburger, T. and co-authors. 2008. Saharan dust absorption and refractive index from aircraft-based observations during SAMUM 2006. *Tellus* **61B**, doi:10.1111/j.1600-0889.2008.00383.x.

Schnaiter, M., Gimmler, M., Llamas, I., Linke, C., Jager, C. and co-authors. 2006. Strong spectral dependence of light absorption by organic carbon particles formed by propane combustion. *Atmos. Chem. Phys.* **6**, 2981–2990.

Sokolik, I. N. and Toon, O. B. 1999. Incorporation of mineralogical composition into models of the radiative properties of mineral aerosol from UV to IR wavelengths. *J. Geophys. Res.* **104**, 9423–9444.

Stratmann, F. and Wiedensohler, A. 1996. A new data inversion algorithm for DMPS-measurements. *J. Aerosol Sci.* **27**, 339–340.

Tegen, I., Lacis, A. A. and Fung, I. 1996. The influence on climate forcing of mineral aerosols from disturbed soils. *Nature* **380**, 419–422.

Tesche, M., Ansmann, A., Müller, D., Althausen, D., Heese, B. and co-authors. 2008. Vertical profiling of Saharan dust with Raman lidars and airborne HSRL in southern Morocco during SAMUM. *Tellus* **61B**, doi:10.1111/j.1600-0889.2008.00390.x.

Wernli, H. and Davies, H. 1997. A Lagrangian-based analysis of extratropical cyclones. I: the method and some applications. *Quart. J. Roy. Met. Soc.* **123**, 467–489.

Wex, H., Neusüss, C., Wendisch, M., Stratmann, F., Koziar, C. and co-authors. 2002. Particle scattering, backscattering, and absorption coefficients: an in-situ closure and sensitivity study. *J. Geophys. Res.* **107** (D21), 8122, doi:10.1029/2000JD000234.

Wiedensohler, A. 1988. An approximation of the bipolar charge distribution for particles in the submicrometer size range. *J. Aerosol Sci.* **19**, 387–389.